Radiation Response of Emerging High Gain/Low Noise Detectors

Heidi N. Becker
Jet Propulsion Laboratory
California Institute of Technology

October 31, 2005

NASA Electronic Parts & Packaging Program
FY05 Sensor Technology (Radiation) Task
NASA UPN: 104-07-01-3
JPL Project: 102197 JPL Task #3.21.4

1.0 Introduction

In previous years, the NEPP Sensor Technology radiation task has examined the radiation response of several classic avalanche photodiode (APD) technologies. Dose effects from high energy protons and Co-60 gamma rays have been reported for silicon (FY03), InGaAs (FY04), and Ge (FY04) APDs that have been under consideration for various applications in current and future NASA missions [1]-[4]. Although classic APDs provide higher gain and better signal to noise performance when compared to many other semiconductor detectors, they still suffer from a relatively high excess noise factor when operated at very high gain. This limits their potential in applications such as interplanetary optical communications, where photon counting at very high gain will be required.

Several novel technologies are being explored by NASA for use in photon counting applications. The near term focus is on ground-based optical communications receivers, but it is expected that the field will naturally progress toward space-born receivers in Earth or Mars orbit. One benefit of space-born receivers is the lack of atmospheric interference. LIDAR applications represent an additional forum for detectors with high detection efficiency. The goal of this radiation study was to begin to understand how space radiation effects will alter the operational performance of candidate technologies prior to the end of their development phase.

Three technologies were examined during FY05:

1. **Silicon Internal Discrete Avalanche "IDA" Photodiodes (a.k.a. Discrete Amplification Detectors "DADs")**
2. **InGaAs/InAlAs Avalanche Photodiodes (operated in Geiger mode)**
3. **InGaAs on Si diodes (operated in Geiger mode)**

Detailed descriptions of each technology, including their advantages over classic APDs, are provided below. Limited sample availability (due to the high cost of engineering samples) required that testing focus on the likely *dominant* area of vulnerability for each technology type, based on historical president and best engineering guesses, given a basic understanding of the design. The testing strategy for each technology is presented. Irradiation levels were chosen based on reasonable expected radiation environments for potential space-borne applications in Earth or Mars orbit.

2.0 Silicon Internal Discrete Avalanche "IDA" Photodiodes (Discrete Amplification Detectors "DAD"s)

2.1 Description of IDA Technology

The excess noise factor (F) is a parameter which quantifies the amplification noise of a detector. It is related to the statistics of gain (M) as follows:

$$F = \frac{\overline{M^2}}{\overline{M}^2} = 1 + \frac{\sigma^2}{\overline{M}^2} \qquad (F = 1 \text{ for an ideal amplifier}) \quad (1)$$

where σ^2 is the variance of the gain. The McIntyre gain probability distribution of classic APDs is relatively broad, particularly at high gains. This leads to typical excess noise factors of 2 or more in silicon APDs at gains of only a few hundred [5]. Although IDA technology uses the same avalanche multiplication process to achieve gains as high as 100,000, its design allows it to overcome the stochastic nature of this amplification mechanism.

In IDA devices, the input signal is separated into multiple *spatially separate* channels, each channel containing the same number of elementary charges. The number of utilized channels is a monotonic function of the size of the input signal. Each discrete packet of elementary charges is multiplied by a given amplification factor, so that a respective number of calibrated, amplified signal packets are read out from the utilized channels. The avalanche multiplication is internally controlled by space charge screening so that each signal packet reaches essentially the same gain. This leads to a very narrow gain distribution and a correspondingly low excess noise factor.

Amplification Technologies, Inc.'s patent (United States Patent 6,885,827) describes an implementation of a discrete amplifier which uses an array of cellular silicon p-n junctions, each junction coupled to an n+ polysilicon conductive channel electrode. The discrete channel electrodes are separated from a common "readout" electrode by an insulator layer which capacitively couples the channel electrodes to the common. The channel electrodes are also coupled to the common by a wide band gap semiconductor plug (such as SiC). Fig. 2.1.1 shows a conceptual sketch of an IDA channel [6].

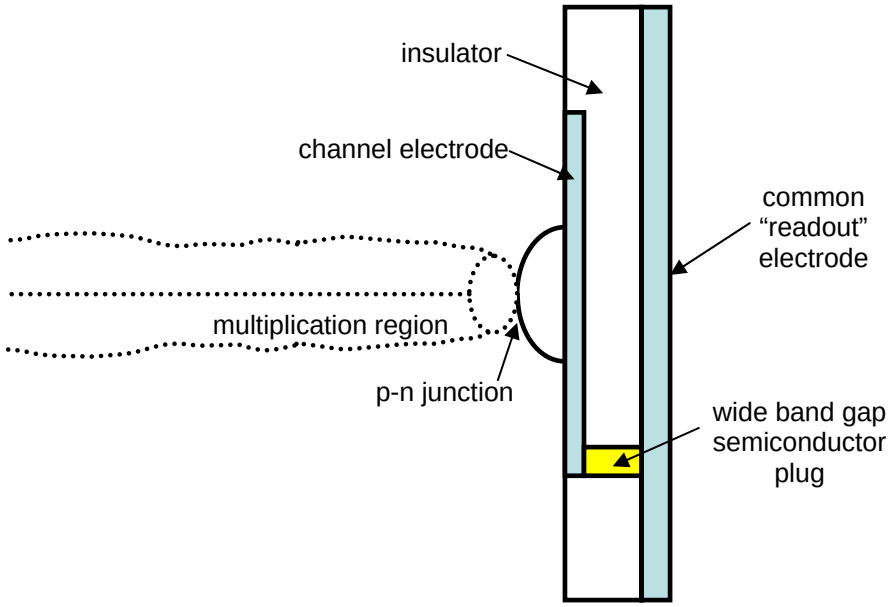

Fig. 2.1.1 Conceptual sketch of a single IDA channel (adapted from U.S. Patent 6,885,827)

The supply voltage is set such that the potential across the avalanche region is slightly larger than the breakdown value. Avalanche multiplication causes electrons to accumulate on the channel electrode, until the field is such that multiplication ends via "negative feedback" (the accumulated charge screens the field). Because the channel electrodes and the common are capacitively coupled, an "image" charge builds up on the common electrode. The build up of amplified signal charge on the channel electrode begins a process where the potentials in the various regions of each channel change. This leads to a switching mechanism that allows the readout of the amplified signal and the reset of the channel to its original state - a high potential across the avalanche region.

2.2 IDA Samples

Although the exact implementation of the discrete amplification mechanism in our engineering samples is proprietary, the tested samples do incorporate cellular Si/SiO_2 interfaces under aluminum contact regions. Focused ion beam etching and electron dispersive spectroscopic (EDS) SEM analysis was performed on

one of the samples. Fig. 2.2.1 is a SEM image of an etched region. Elemental analysis confirmed the presence of an oxide layer between the aluminum electrode region and the "floating" mesa regions to either side of the center contact. The mesa regions have a high silicon content and may be polysilicon channel electrodes for two adjacent amplification channels. Figure 2.2.2 shows a wider view of the etched region.

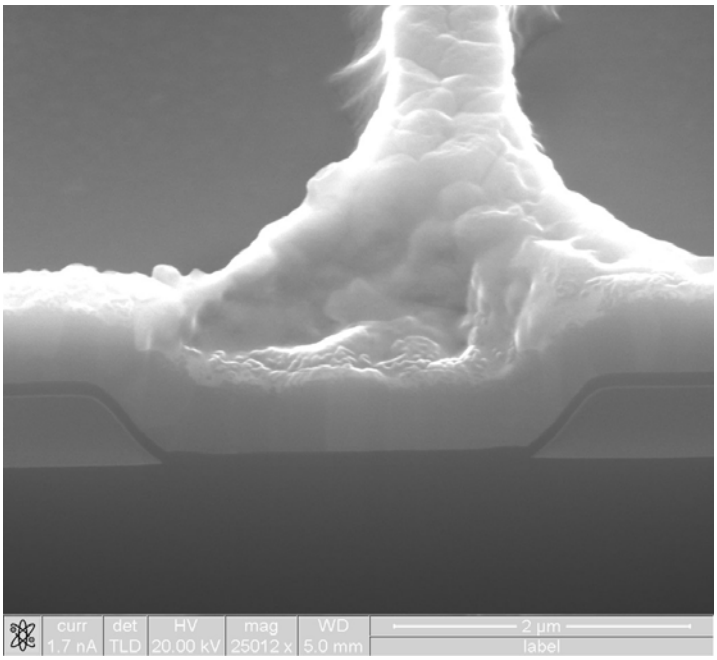

Fig. 2.2.1 SEM image of a FIB-etched IDA sample. The two floating "mesa" regions are separated from the aluminum contact by an oxide layer.

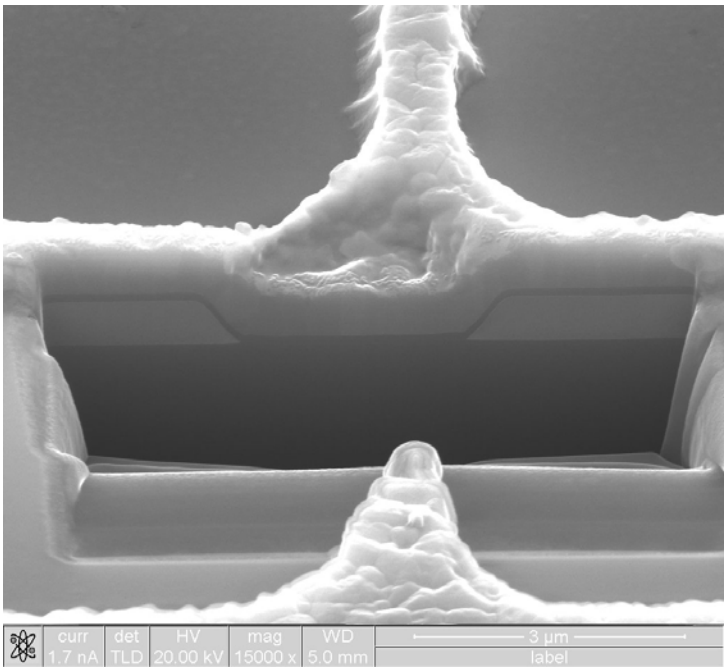

Fig. 2.2.2 A wider view of the etched region.

Figure 2.2.3 is an optical microscope image of the IDA die. The cellular nature of the active region can be seen.

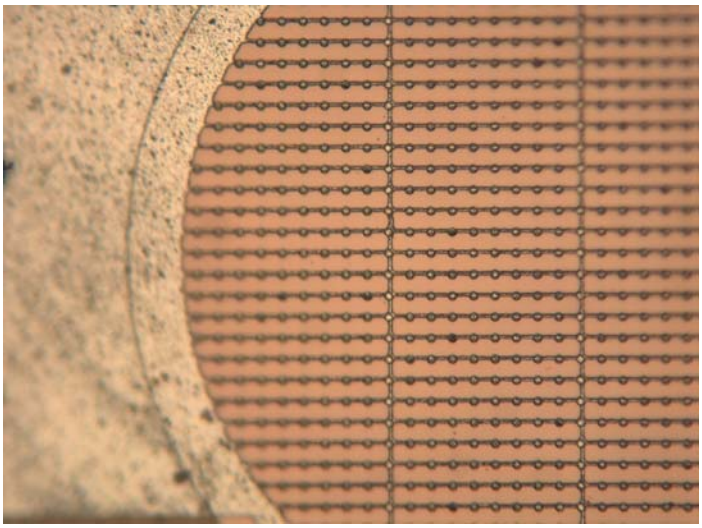

Fig. 2.2.3 Optical microscope image of the "cellular" IDA structure.

Three engineering samples of the silicon IDA technology were available for testing, having already been characterized at JPL's Optical Communications Detector and Receiver Calibration Facility. As illustrated above, the structure that allows IDA technology to have such superior gain and noise characteristics, compared to classic APDs, is also proportionally more complex than a classic APD. Limited sample availability required that testing focus on the expected first-order vulnerability. Previous testing of silicon and near infrared APDs for NEPP with protons and Co-60 gamma rays indicated that bulk displacement damage effects are a major contributor to APD degradation, particularly affecting increases in dark current. However, because of the dependence of the IDA switching mechanism on various potentials within the amplification channels (and the importance of the oxide layer that capacitively couples individual channel electrodes to the readout electrode), it was decided to focus the radiation testing effort on the impact of ionization damage. It was suspected that trapped charge and/or interface traps could have a significant influence on IDA functionality.

2.3 IDA Test Methodology

Irradiations were performed at JPL's high dose rate Co-60 gamma facility, using a 50 rad(Si)/s dose rate. The IDA samples were irradiated at ambient temperature while under bias. The static bias used during irradiation was chosen based on the bias condition that yielded the best operational performance prior to irradiation, but was adjusted down by several volts to protect the samples; it was not known whether a potentially damaging high current condition would result from irradiating the IDA technology under bias, so a conservative approach was taken. The first post-irradiation characterizations were performed less than 2 hours after irradiation.

Devices were characterized prior to and following irradiation in JPL's Optical Communications Detector and Receiver Calibration Facility. The characterizations were performed with the samples in a light-tight dewar at 295K. 850 nm light was fed into the dewar through a fiber optic cable and collimated before illuminating the IDA active region. Figure 2.3.1 shows the test bed schematic. The IDA output was split so that pulses could simultaneously be monitored on a digital storage oscilloscope (DSO) and processed by "ppM-DTS" software which determined pulse amplitude statistics and count rates. Figure 2.3.2 shows the IDA test fixture inside one of JPL's dewars.

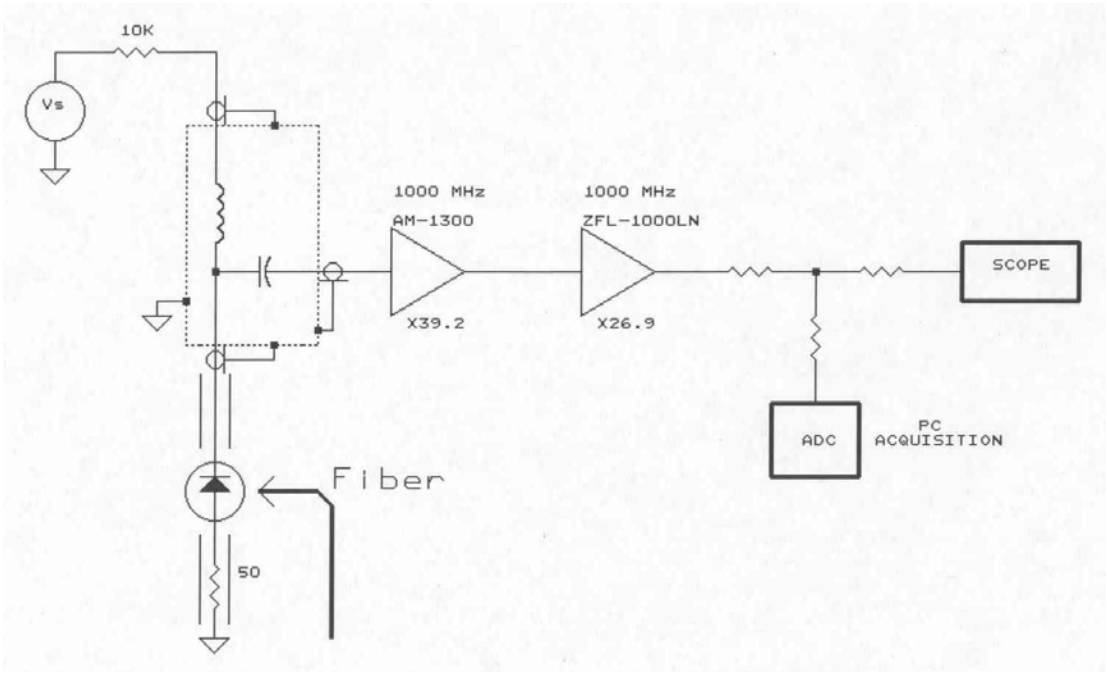

Fig. 2.3.1 Schematic for IDA test bed.

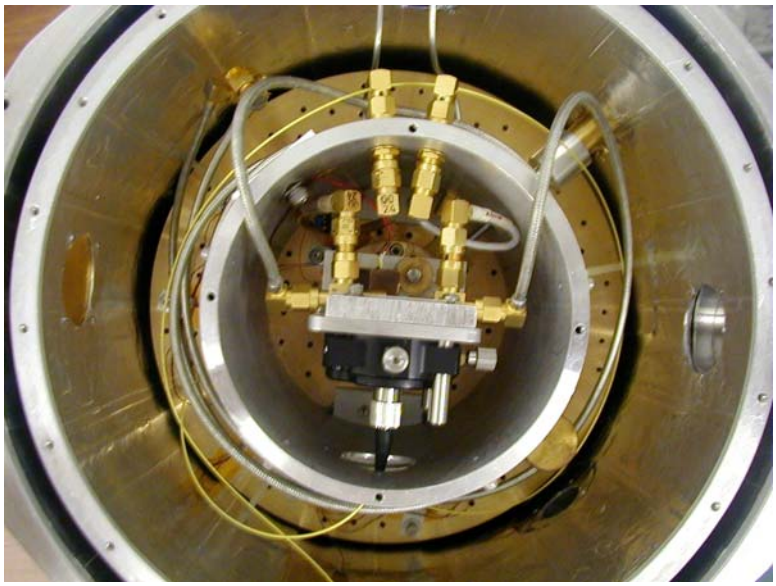

Fig. 2.3.2 IDA test fixture (the fiber optic cable is coupled to the detector under test; an x-y translation stage is used for alignment)

The emphasis of the sample characterization was placed on counting statistics. Dark count rates, count rates under 850 nm illumination, the mean and standard deviation of the pulse amplitudes, and pulse width statistics were examined. The excess noise factor was determined prior to and following irradiation. Prior to irradiation, the supply voltage that yielded the optimal operational mode (at 295K) was determined. Post-irradiation mode changes under the same bias, temperature, and photon flux were examined for each sample.

2.4 IDA Test Results:

The three engineering samples were characterized prior to irradiation, and the results compared to those taken when the devices were originally characterized by JPL (~1 year earlier). Irradiation was first performed on the sample with the least optimal performance to get a feel for the post-irradiation trend, and any annealing effects. The behavior of this sample (2C) following irradiation ended up being unique (a *decrease* in dark current and a *sharper* pulse amplitude distribution was observed *following irradiation*!); this odd behavior may be related to ageing effects in this particular sample (our engineering samples had un-passivated die). Samples 2C-10 and 2M showed similar post radiation mode shifts. 2M exhibited the most optimal performance prior to irradiation, so its post-irradiation behavior is considered most representative of radiation-induced degradation effects in this technology; results for 2M are highlighted for the remainder of the report.

Note on the detection efficiency of 2M: Initial characterization with 697 nm photons showed detection efficiencies of 24-30%, depending on the supply voltage applied to the sample. The relatively low detection efficiency observed with 850 nm photons (< 1%) is not understood, since silicon would be expected to have a higher detection probability at this wavelength. It is unlikely that an ageing effect could be responsible, and we don't believe that the low detection efficiency at 850 nm is due to an alignment issue.

2.4.1 Pre-irradiation Performance

Prior to irradiation, the optimal operational mode (at 295K) was found when a supply voltage of 80V was applied. Under these conditions, the excess noise factor was 1.09, and pulse widths were narrow (< 1 ns). Figure 2.4.1 shows an oscilloscope frame that was saved during pre-irradiation illumination of 2M with 850 nm photons. The pulse amplitude uniformity, which results in such a low excess noise factor in this technology, can clearly be seen. Figure 2.4.2 illustrates the narrow pulse width prior to irradiation.

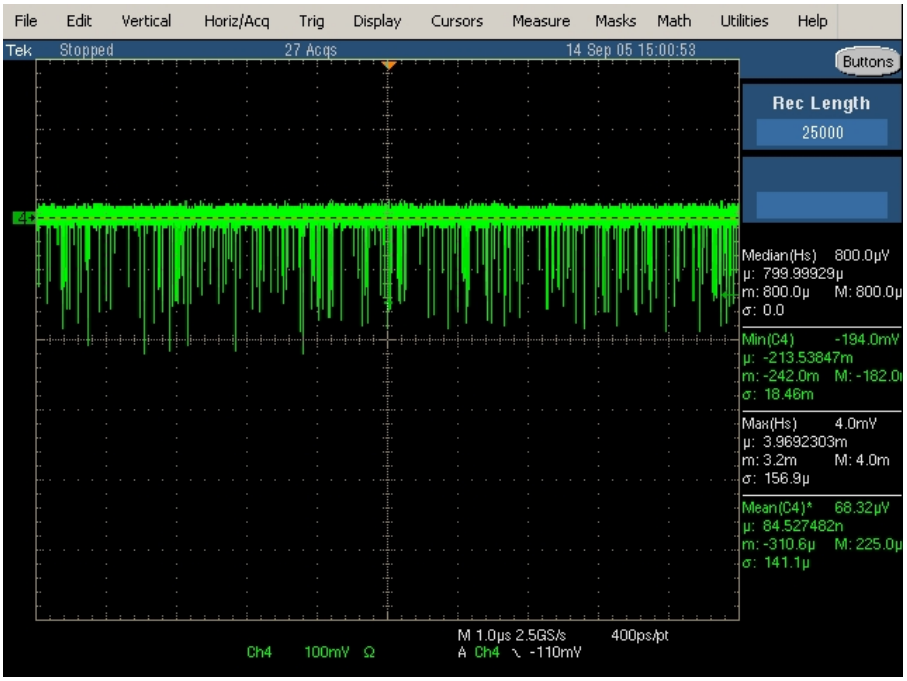

Fig. 2.4.1 Pulses during illumination with 850nm photons prior to irradiation (sample "2M").

Fig. 2.4.2 Single photon pulse prior to irradiation.

Figure 2.4.3 shows a screen save of the ppM-DTS software during pre-rad characterization of 2M. The small peak in the plot is the pre-irradiation pulse amplitude distribution at 295K with V_s=80V. Pulse amplitude statistics and total counts per second are listed in the right bar of the data acquisition software.

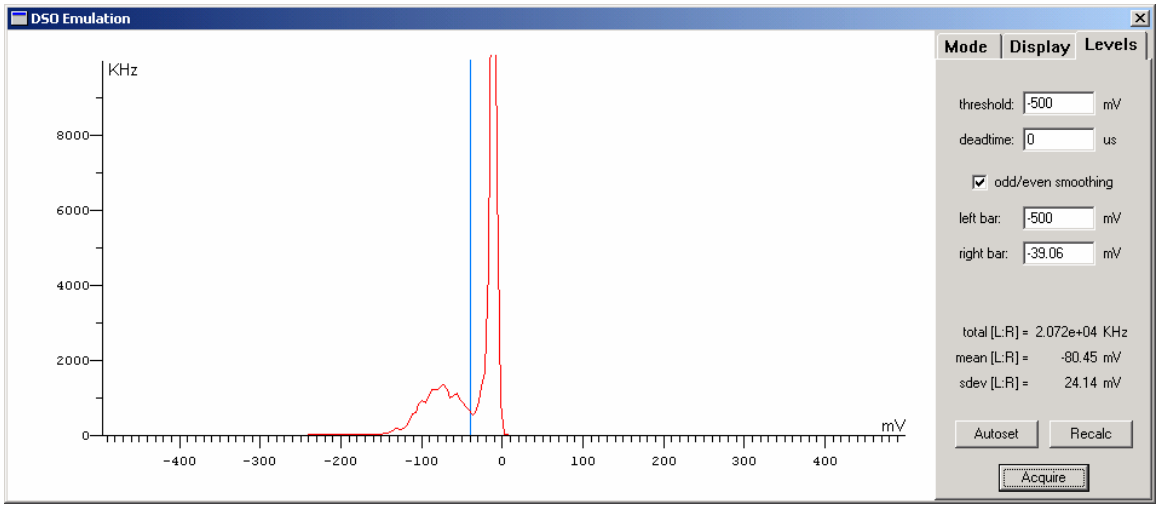

Fig. 2.4.3 Pulse amplitude distribution for IDA sample 2M, as recorded by ppM-DTS acquisition software. The operational conditions were: 295K, Vs=80V, 850 nm illumination.

2.4.2 Post-irradiation Performance

Following irradiation to 5 krad(Si), a significant mode shift was observed at the operational conditions used for the pre-irradiation characterization. Inverted (positive) pulses and a general broadening of the pulse width were observed. Figure 2.4.4 shows the very different pulse characteristics following irradiation. The pulse amplitude statistics were corrupted by the presence of many inverted (positive) pulses.

Fig. 2.4.4 Pulses following irradiation with Co-60 gammas to 5 krad(Si).
The same operational conditions were used as in Fig.'s 2.4.1 and 2.4.2.

The supply voltage was gradually reduced to try to find a mode of operation similar to that achieved prior to irradiation. At 79V, no inverted pulses were observed, but the average pulse width under illumination was still over 11ns (σ=32.29 ns), and the count rate was two orders of magnitude less than what could be achieved prior to irradiation. Fig. 2.4.5 shows the pulse amplitude histogram at 79V.

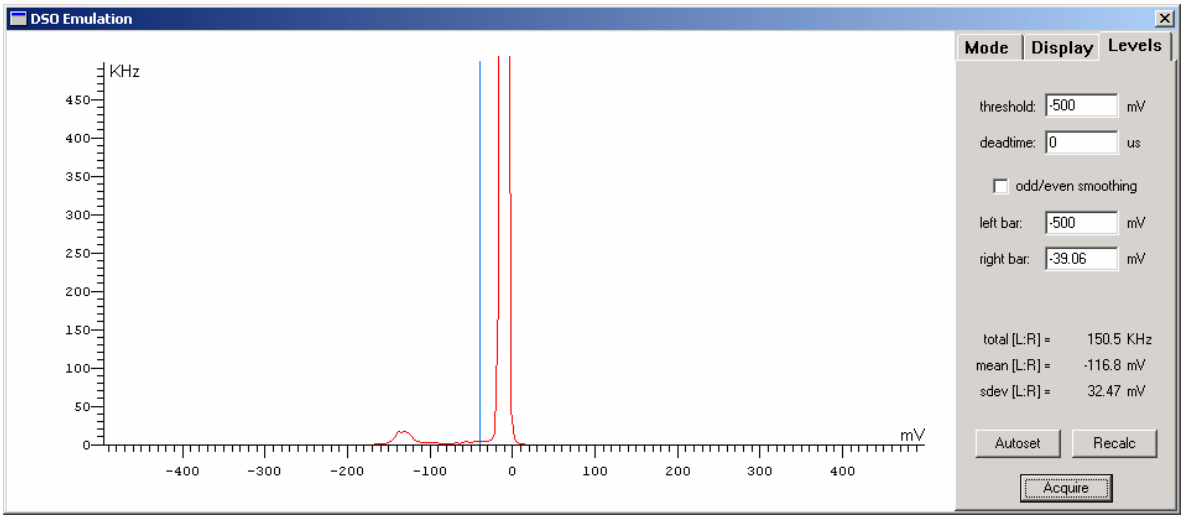

Fig. 2.4.5 Pulse amplitude distribution for AT sample 2M. The operational conditions were: 295K, Vs=79V, 850 nm illumination. Radiation dose = 5 krad(Si).

Sub-nanosecond pulse widths were observed when the supply voltage was reduced to 78.6V. However, the corresponding count rate was only 8.9 * 10^3 counts/s, and the dark count rate was only 60 counts/s. When the supply voltage was reduced to 78.1V, no counts were observed at all.

2.4.3 Annealing Effects

Because the performance of 2M had so significantly changed by 5 krad(Si), it was decided to not irradiate the sample to higher levels of ionizing dose and focus instead on any annealing behavior that might be observed as a function of time. The device was allowed to reach ambient temperature and sit with V_s=0. The sample was characterized again 6 hours, 24 hours, and 1 month after the first post-irradiation characterization. The observed trend over the 1 month annealing period was a gradual decrease in the supply voltage required to put the sample into the broad inverted pulse mode. Figure 2.4.6 shows pulses for V_s=76.1V after the 1 month anneal.

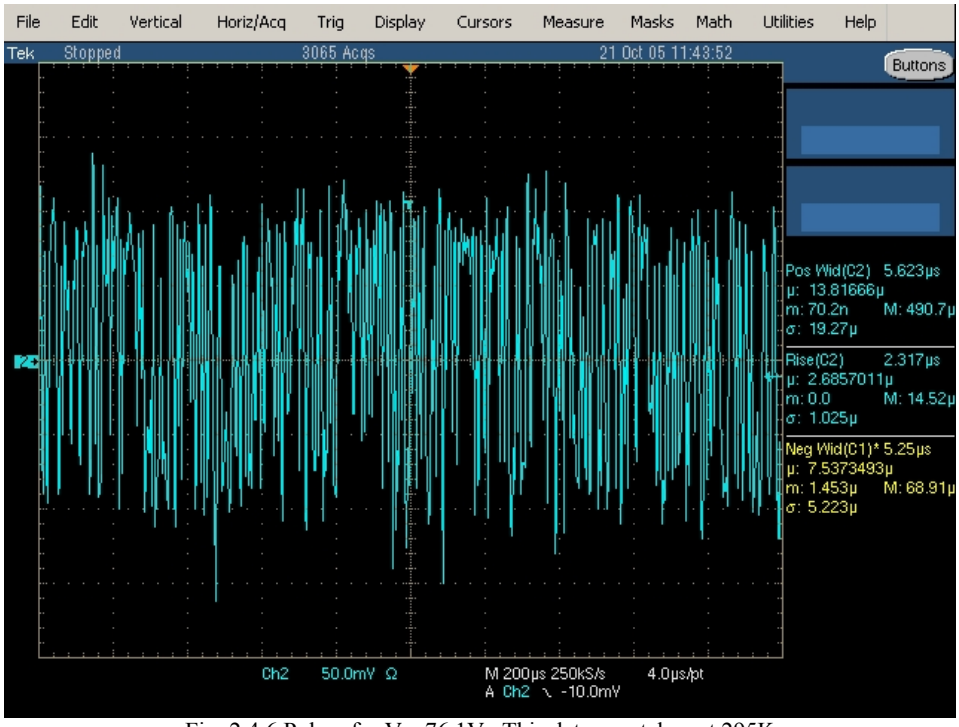

Fig. 2.4.6 Pulses for Vs=76.1V. This data was taken at 295K
1 month after irradiation to 5 krad(Si).

Table 2.4 lists several performance parameters for IDA sample 2M. Values taken during pre- and post-irradiation characterization, including post-annealing characterizations, are presented. The table illustrates that the supply voltage necessary to invert the pulses is decreasing over the annealing period. It can also be seen that the irradiation caused a reduction in the illuminated *and* dark count rates, along with a broadening of the average pulse width. It is interesting to note that the radiation damage *did not increase the excess noise factor* or dramatically change the average pulse amplitude.

Table 2.4 Performance Parameters for AT sample "2M"

Radiation level	V_s above which *inverted pulses* were observed (V)	Optimal Supply voltage [*non-inverted pulses*] (V)	Dark count rate (cps)	Count rate (cps)	Excess Noise Factor	Pulse width (ns)	Mean pulse amplitude [50 Ohm, 500X amplification, 1GHz BW] (mV)
0 krad	-	80-82	~$4*10^4$	$2.1*10^7$-$3.4*10^7$	1.09-1.10	<1	80-100
5 krad	79	79	477	$1.5*10^5$	1.08	11(avg)/ 32(σ)	117
		78.6	60	$8.9*10^3$	1.06	<1	56
		78.1	0	0	-	-	-
5 krad & 24 hour anneal	78	76.2	0	$1.3*10^5$	1.01	26 (avg)	138
5 krad & 1 month anneal	76	75.4	0	$2.8*10^6$	1.04	18 (avg)	91

2.5 Conclusions

It can be surmised that the reduced count rate observed following ionizing dose testing is due to the introduction of bulk charge traps and interface traps at the SiO_2/Si interface(s). A relatively thick oxide (~100 nm) is used between the aluminum contact and the floating mesa regions described in Section 2.2, so charge trapping and interface traps are expected to be fairly significant. This may be screening the field in the amplification region so that a larger number of accumulated carriers are required at the channel electrode to quench the amplification process. This may occur over a significantly longer period of time than in an un-irradiated sample, and may even require multiple channel inputs before amplification finally ceases. The broadened pulse widths indicate that the readout mechanism is also impacted by ionizing dose. The potentials within each channel that control the switching/readout mechanism have probably been quite altered by ionizing dose, enough to affect the timing.

It is interesting that the excess noise factor remains low following irradiation (although the count rate is greatly decreased). This is probably because the amount of signal amplification that occurs before readout is a function of the capacity of the insulator layer between the channel electrodes and the common. Ionizing dose does not appear to be affecting the capacity, since similar pulse amplitudes were observed before and after the irradiation.

The "reverse" annealing observed over the month that the device was allowed to sit unbiased was not expected. However, it is likely that any migration of charge during this period was very subtle. If we compare dark IV curves for 2M taken at the various steps in the experiment (Figure 2.5.1), we see that the "knee" became much sharper following irradiation. This knee drifted down and to the left (towards lower biases) with time. This is consistent with a breakdown mode occurring at lower supply voltages over time. However, note that the decreases in dark current at voltages below breakdown were rather small.

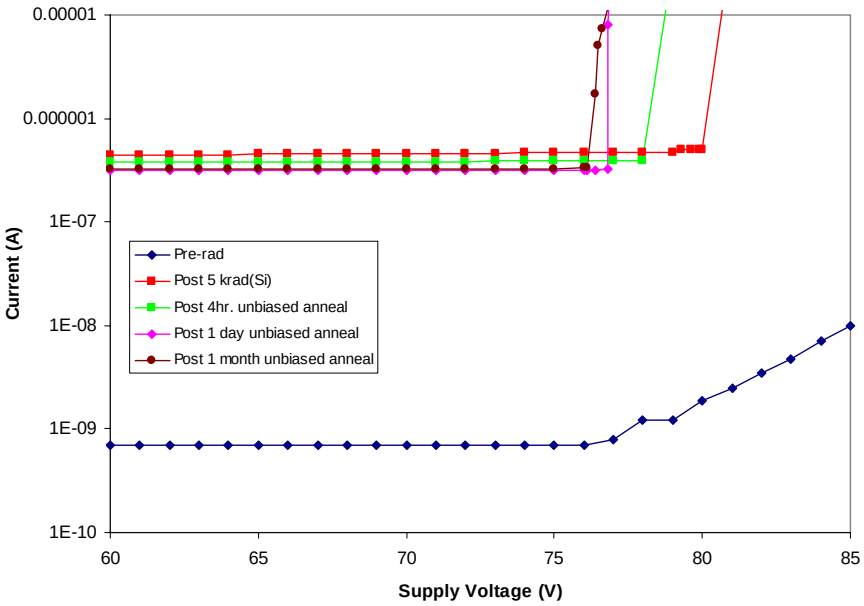

Fig. 2.5.1 Dark IV curves for 2M at various steps in the experiment.

Future radiation testing of the IDA technology could be performed with test samples irradiated unbiased, to see if this lessens the impact on device functionality. The biased irradiations used in our study may represent the worst case for this technology, as is often the case for CMOS devices. Biased anneals at room temperature, and high temperature anneals could also be performed to see if this improves recovery. Changing the operational temperature may also influence the post-irradiation modes of operation, and this could be explored. This technology should also be tested to lower levels of ionizing dose, and screened for displacement damage effects (displacement damage could affect the operation of the wide band gap semiconductor plug). It is also possible that other implementations of the IDA concept may be more radiation tolerant.

3.0 InGaAs/InAlAs Avalanche Photodiodes (operated in Geiger mode)

3.1 Description of InAlAs APD Technology

InAlAs APDs use an *InAlAs avalanche layer* in place of the InP avalanche layer that is used in conventional InP/InGaAs APDs. The technology has an InGaAs absorption layer, similar to a conventional InP/InGaAs APD. However, unlike an InP/InGaAs APD, the absorption layer is not depleted and no impact ionization occurs within it [7]. The undepleted absorption layer and InAlAs/InGaAs material system has a lower dark current (and excess noise factor) than InP/InGaAs APDs. Lower excess noise (a narrow pulse amplitude distribution) allows the use of a lower discriminator threshold for rejecting dark counts; this increases photon counting efficiency [8].

3.2 Samples

Two Spectrolab InAlAs APD prototypes were available for testing. The samples were 200 μm diameter, front-illuminated avalanche photodiodes fabricated for NASA/JPL. Because of their structural similarity to InP/InGaAs APDs, it was decided to focus the radiation testing effort on displacement damage effects caused by high energy protons. Comparative proton and Co-60 gamma testing of InP/InGaAs APDs for

NEPP in FY04 showed displacement damage to be the dominant contributor to device degradation, particularly effecting dark current increases.

3.3 InAlAs APD Test Methodology

Irradiations were performed using 51-MeV protons. Sample "#1" was irradiated to 6.25 x 10^{10} p/cm^2 and returned to JPL's cryogenic test bed for characterization. A second irradiation was performed one month later to bring the cumulative fluence to 1.25 x 10^{11} p/cm^2, after which the sample was again returned to JPL for characterization. Sample "#2" was irradiated to 3.1 x 10^{10} p/cm^2 because significant degradation was observed in sample #1 after 6.25 x 10^{10} p/cm^2. Both samples were irradiated unbiased, with all leads grounded, at ambient temperature.

The samples were characterized prior to and following irradiation in Jet Propulsion Laboratory's Optical Communications Detector and Receiver Calibration Facility. Characterizations were performed in a light-tight dewar at temperatures ranging from 100-297K. IV curves were taken in the dark and under 1064 and 1534 nm illumination. Counts per second were recorded under several flux levels of 1064 nm and 1534 nm photons. An active quenching circuit was used to apply 5-ns 2.5V pulses, with a 100 kHz rep rate, on top of the dc supply voltage. At supply voltages close to the knee in the detector's IV curve, the extra potential provided by these pulses is enough to put the detector into Geiger mode (V_s > than breakdown voltage) for 5-ns periods. While in Geiger mode, the avalanche multiplication is extreme, gain is very high, and the detector is able to count photons. Figure 3.3.1 is a diagram of the characterization system. Count rates were recorded while the detector under test was illuminated in the pulsed Geiger mode.

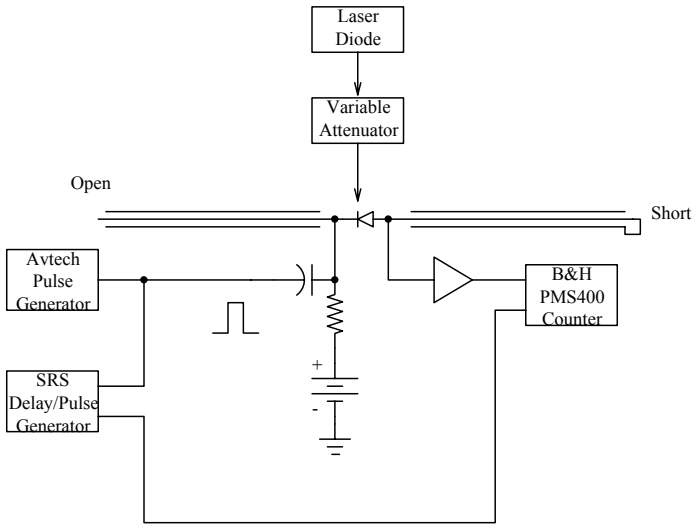

Pulse biased APD with transient cancellation

Fig. 3.3.1 InAlAs APD characterization system

3.4 InAlAs APD Results

Reduced photon count rates were observed following the proton irradiations. After 6.25 x 10^{10} p/cm^2 and 1.25 x 10^{11} p/cm^2, the count rates under 1064 nm and 1534 nm illumination were negligible compared to the corresponding dark count rates. This was the case over the full temperature range used for the

characterizations (100K to 297K). Increasing the photon flux did not improve the count rates, since the dark count rate was already high enough to saturate the 100 kHz digitizer.

Figure 3.4.1 shows count rates for sample #1 at 200K. Dark count rates and count rates under 1064 nm photon illumination are compared for pre- and post-irradiation conditions. Prior to irradiation, the maximum detection efficiency was 4.1% (achieved at a supply voltage of 36.5V). The proton fluence represented in Fig. 3.4.1 is 1.25 x 10^{11} p/cm^2 (the highest used in this study).

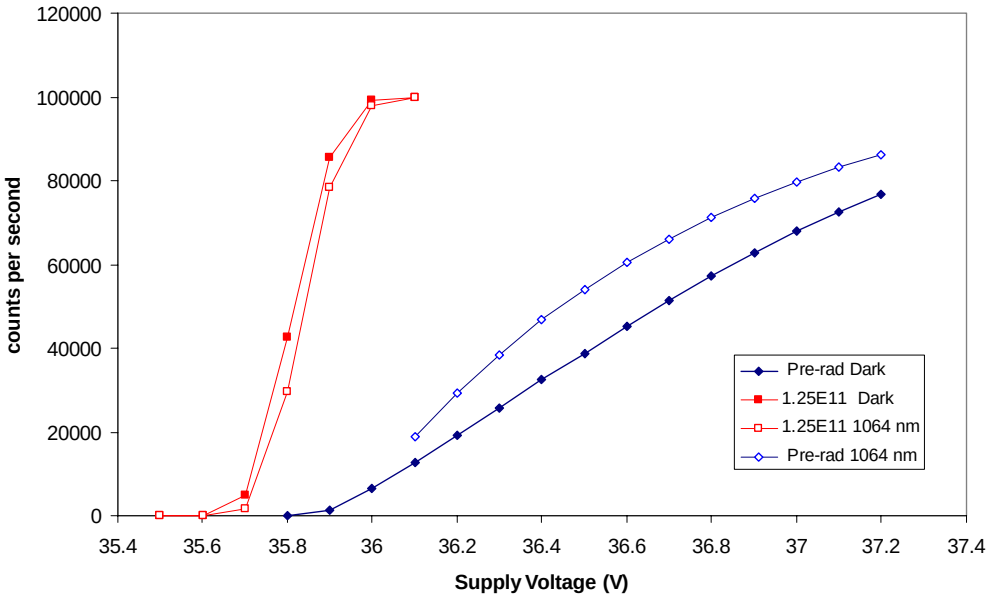

Fig. 3.4.1 Pre- and post-irradiation count rates for Spectrolab sample #1 at 200K.
The maximum pre-irradiation detection efficiency was 4.1% at 36.5V.

There is a dramatic increase in the dark count rate following this fluence, and the count rate under illumination is actually slightly *lower*. It is not presently understood why the rates under illumination would be less, but a similar effect has been observed in un-irradiated devices when comparing dark current to photocurrent at low supply currents [8]. Following this radiation level, the detection efficiency was zero at 200K. At 100K, the detection efficiency (1064 nm) was 9.1% at 33.7V prior to irradiation. After a proton fluence of 1.25 x 10^{11} p/cm^2 the maximum detection efficiency was only 0.8% (at 34.2V).

Figure 3.4.2 shows IV curves for sample #1 at 200K. Prior to irradiation, the dark IV curve had a fairly distinct "knee" near the breakdown voltage of the device. Following irradiation to 1.25 x 10^{11} p/cm^2, a pronounced softening of the knee was observed, along with decreased photocurrent values above the punch through voltage (~20V). These two effects are attributed to an increased number of displacement-damage-induced generation and recombination centers, respectively. There is a much smaller difference between the dark current and photocurrent near the breakdown voltage, which is consistent with the reduced counting efficiency that was observed at this fluence.

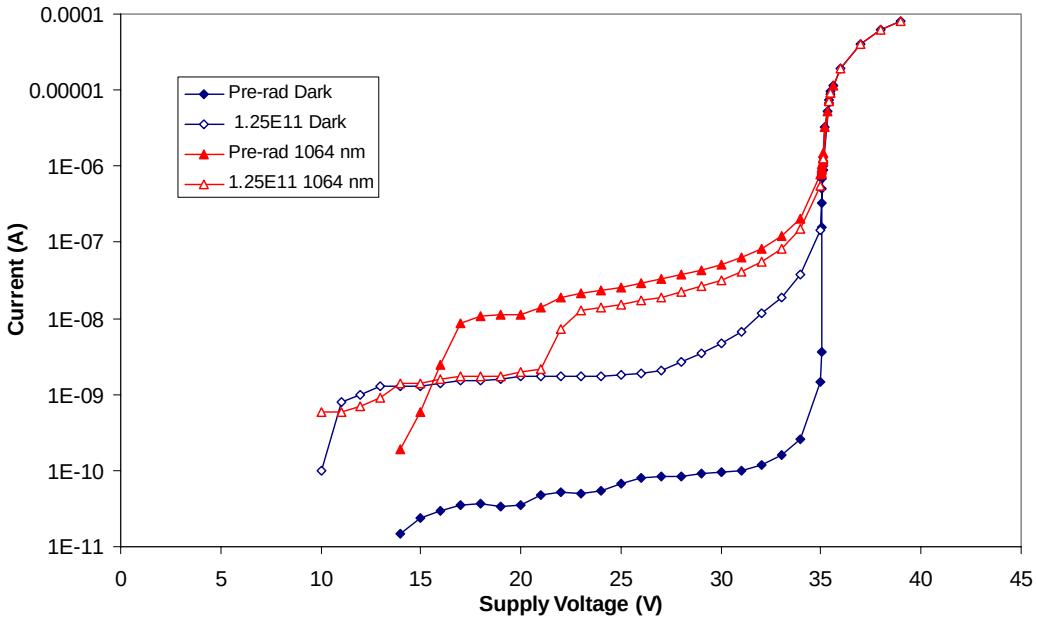

Fig. 3.4.2 Pre- and post-irradiation IV curves for Spectrolab sample #1 at 200K.

The detection efficiency of sample #1 was less than 2% (1064 nm, 100K), following its first irradiation level (6.25 x 10^{10} p/cm^2). Because such decreased detection efficiency was seen in sample #1, the second engineering unit was irradiated to a proton fluence of only 3x10^{10} p/cm^2.

At 200K, sample #2 showed similar degradation in counting efficiency to what had been observed in sample #1. Figure 3.4.3 shows pre- and post-irradiation counts for sample #2 at 200K (1534 nm) following 3 x 10^{10} p/cm^2.

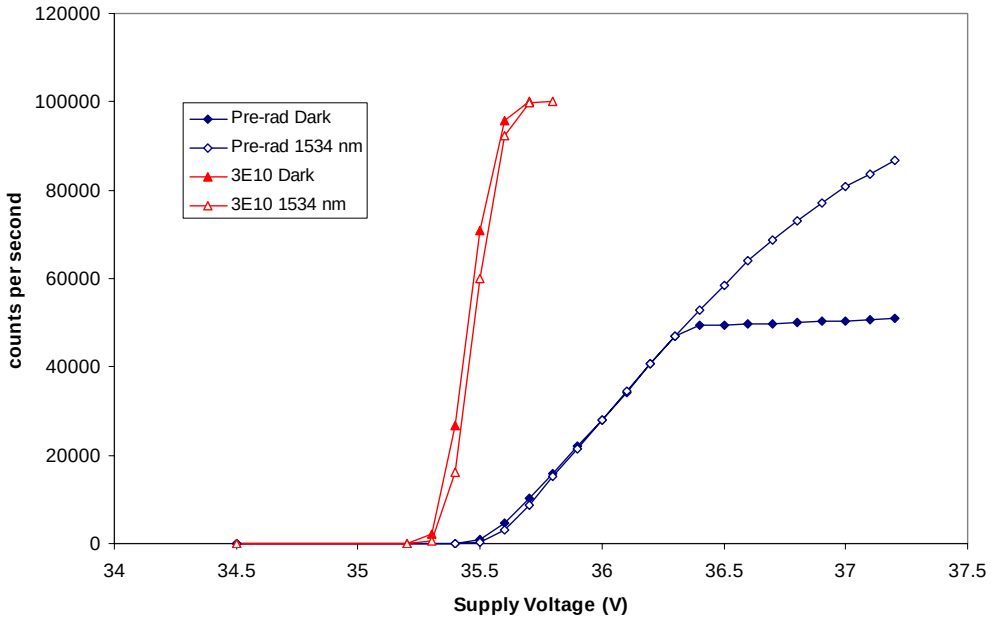

Fig. 3.4.3 Pre- and post-irradiation count rates for Spectrolab sample #2 at 200K (1534 nm).

Photon counting was observed when the temperature of sample #2 was dropped to 100K, however the count rate was significantly reduced compared to that seen before irradiation. Fig. 3.4.4 compares count rates for sample #2 at 100K (1534 nm).

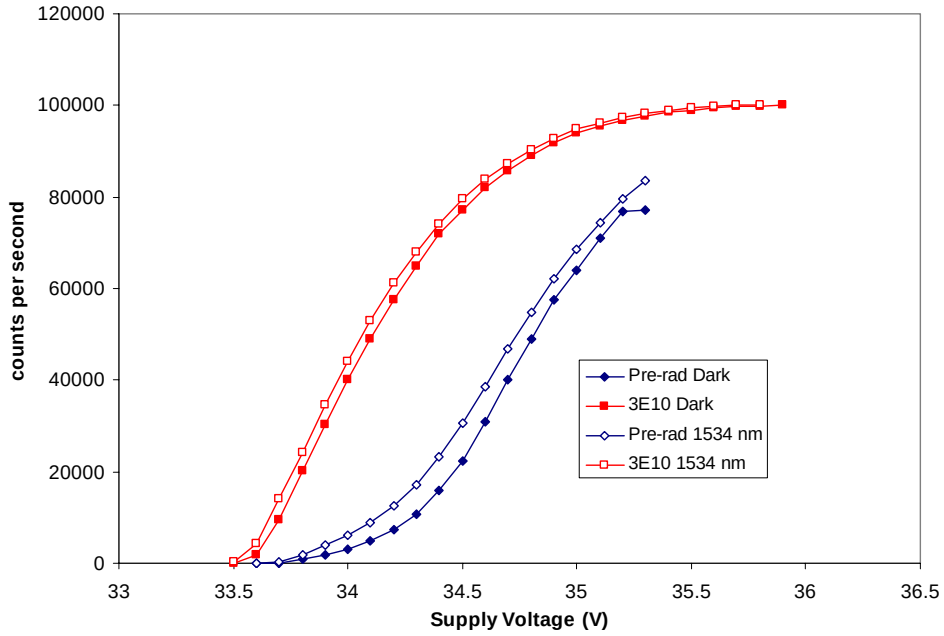

Fig. 3.4.4 Pre- and post-irradiation count rates for Spectrolab sample #2 at 100K (1534 nm).

3.5 Conclusions

The detection efficiency of InAlAs APDs (operated in Geiger mode) was observed to be very sensitive to damage from proton irradiation, although improved efficiency was observed by reducing the temperature to 100K. Displacement damage effects are assumed to be responsible for the degradation, however total ionizing dose testing could be performed in the future to separate out any degradation effects caused by ionization damage. The reduced detection efficiency and softening of the IV curves can be attributed to and increased number of generation centers following proton irradiation.

The proton fluences used in our study are moderate compared to the displacement damage dose requirements of many missions in LEO or Mars orbit. Further testing at lower levels of displacement damage dose would be desirable to determine doses where changes in detection efficiency would be small enough to not be mission critical.

4.0 InGaAs on Silicon diodes (operated in Geiger mode)

4.1 Description of InGaAs on Silicon Technology

InGaAs on silicon APDs use an InGaAs absorption layer fused to a silicon multiplication layer. This combination allows both high quantum efficiency in the near infrared (the InGaAs absorber) and low-noise gain. The silicon avalanche region exploits the relatively low ionization coefficient "k" of silicon compared to InGaAs, which results in a lower excess noise factor. Unfortunately, this technology has a

known issue with hysteresis near the breakdown voltage [8]. Figure 4.1.1 shows IV curves taken at 100K for a JPL InGaAs on silicon engineering sample. The hysteresis effect can clearly be seen.

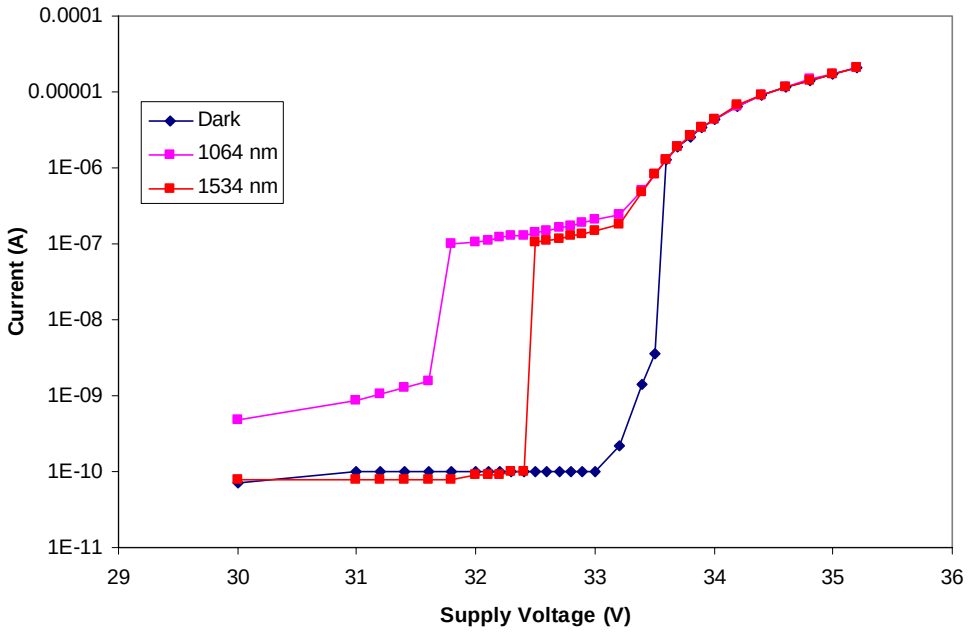

Fig. 4.1.1 IV curves for an InGaAs on silicon engineering sample prior to irradiation.

4.2 InGaAs on Si Results

The same approach used to characterize the InAlAs APDs was used for the InGaAs on Si technology. We were unable to get this sample to count photons during the pre-irradiation characterization, which may be related to the hysteresis issue. The intention of the radiation campaign was to characterize this technology for displacement damage dose (DDD) effects from 51-MeV protons. Unfortunately, the sample suffered a catastrophic failure (dead short) following the first 51-MeV proton fluence level of 6.25 x 10^{10} p/cm^2. Because of the poor pre-irradiation performance in photon counting mode, it was decided to place more focus on the other two technologies in our study, in lieu of investigating the failure mechanism.

5.0 Summary

We have performed preliminary radiation experiments on three emerging high gain/low noise detectors. Our results indicate that these technologies would be fairly sensitive to radiation effects in a space-born application. Silicon internal discrete avalanche photodiodes experienced significant mode shifts after irradiation to 5 krad(Si), and InAlAs APDs showed large reductions in detection efficiency after 51-MeV proton fluences of 3 x 10^{10} p/cm^2. However, there is room for additional radiation characterization to determine the worst case operational conditions during irradiation (for the IDA technology), possible beneficial annealing effects from bias or temperature (IDA), and testing could be performed to lower cumulative levels of DDD and TID than explored here, in order to bound performance degradation from dose effects.

6.0 Acknowledgements

Engineering samples and technical consultation were provided by William H. Farr, Work Area Manager for Optical Communications Receivers at the Jet Propulsion Laboratory. David Zhu of the Jet Propulsion Laboratory is gratefully acknowledged for technical support with detector characterization. Ron Ruiz is thanked for focused ion beam etching and scanning electron microscope analysis of the IDA technology. This research was carried out at the Jet Propulsion Laboratory, California Institute of Technology, under a contract with the National Aeronautics and Space Administration as part of the NASA Electronic Parts and Packaging Program, Code Q. Reference herein to any specific commercial product, process, or service by trade name, trademark, manufacturer, or otherwise, does not constitute or imply its endorsement by the United States Government or the Jet Propulsion Laboratory, California Institute of Technology.

7.0 References

[1] H.N. Becker, "FY04 NEPP TRO – Sensor Technology: Near Infrared Avalanche Photodiodes," October, 2004.

[2] H.N. Becker and A.H. Johnston, "Dark current degradation of near infrared avalanche photodiodes from proton irradiation," *IEEE Trans. Nucl. Sci*., vol. 51, no. 6, pp. 3572-3578, Dec. 2004.

[3] H.N. Becker, T.F. Miyahira, and A.H. Johnston, "The Influence of Structural Characteristics on the Response of Silicon Avalanche Photodiodes to Proton Irradiation," *IEEE Trans. Nucl. Sci*., vol. 50, no. 6, pp. 1974-1981, Dec. 2003.

[4] H.N. Becker, "FY03 NEPP TRO – Improved Radiation Qualification & Test Methods: Optical Detector Noise Characterization (Avalanche Photodiodes)," September, 2003.

[5] A.V. Krutov, E.E. Godik, and W. Seemungal, "Highly sensitive silicon photodetectors with internal discrete amplification," *Proc. of SPIE*, vol. 5353, pp. 29-35, 2004.

[6] D.A. Shushakov and V.E. Shubin, United States Patent 6,885,827, April 26, 2005 (http://www.uspto.gov/, Sept. 19, 2005).

[7] N. Li, et al., "InGaAs/InAlAs avalanche photodiode with undepleted absorber," *Applied Physics Letters*, vol. 82, no. 13, pp. 2175-2177, March 31, 2003.

[8] M.A. Krainak, "Photon Counting Detectors for the 1.0-2.0 Micron Wavelength Range," http://esto.nasa.gov/conferences/estc2004/papers/b3p1.pdf, April 29, 2005.